

## DARK MATTER ANNIHILATION AND PRIMORDIAL STAR FORMATION

ARAVIND NATARAJAN

Fakultät für Physik, Universität Bielefeld, Universitätsstraße 25, Bielefeld D-33615, Germany  
anatarajan@physik.uni-bielefeld.de

JONATHAN C. TAN

Department of Astronomy, University of Florida, Gainesville, FL 32611, U.S.A.  
jt@astro.ufl.edu

BRIAN W. O'SHEA

oshea@msu.edu

Department of Physics &amp; Astronomy, Michigan State University, East Lansing, MI 48864, U.S.A.

*Submitted to ApJ*

## ABSTRACT

We investigate the effects of weakly-interacting massive particle (WIMP) dark matter annihilation on the formation of Population III.1 stars, which are theorized to form from the collapse of gas cores at the centers of dark matter minihalos. We consider the relative importance of cooling due to baryonic radiative processes and heating due to WIMP annihilation. We analyze the dark matter and gas profiles of several halos formed in cosmological-scale numerical simulations. The heating rate depends sensitively on the dark matter density profile, which we approximate with a power law  $\rho_\chi \propto r^{-\alpha_\chi}$ , in the numerically unresolved inner regions of the halo. If we assume a self-similar structure so that  $\alpha_\chi \simeq 1.5$  as measured on the resolved scales  $\sim 1$  pc, then for a fiducial WIMP mass of 100 GeV, the heating rate is typically much smaller ( $< 10^{-3}$ ) than the cooling rate for densities up to  $n_{\text{H}} = 10^{17} \text{ cm}^{-3}$ . In one case, where  $\alpha_\chi = 1.65$ , the heating rate becomes similar to the cooling rate by a density of  $n_{\text{H}} = 10^{15} \text{ cm}^{-3}$ . The dark matter density profile is expected to steepen in the central baryon-dominated region  $\lesssim 1$  pc due to adiabatic contraction, and we observe this effect (though with relatively low resolution) in our numerical models. From these we estimate  $\alpha_\chi \simeq 2.0$ . The heating now dominates cooling above  $n_{\text{H}} \simeq 10^{14} \text{ cm}^{-3}$ , in agreement with the previous study of Spolyar, Freese & Gondolo. We expect this leads to the formation of an equilibrium structure with a baryonic and dark matter density distribution exhibiting a flattened central core. Examining such equilibria, we find total luminosities due to WIMP annihilation are relatively constant and  $\sim 10^3 L_\odot$ , set by the radiative luminosity of the baryonic core. We discuss the implications for Pop III.1 star formation, particularly the subsequent growth and evolution of the protostar. Even if the initial protostar fails to accumulate any additional dark matter, its contraction to the main sequence could be significantly delayed by WIMP annihilation heating, potentially raising the mass scale of Pop III.1 stars to masses  $\gg 100 M_\odot$ .

*Subject headings:* cosmology: theory — dark matter — early universe — galaxies: formation — stars: formation

## 1. INTRODUCTION

Population III stars are defined to be those whose formation and evolution are independent of metallicity (McKee & Tan 2008; O'Shea et al. 2008), since their metallicity is extremely low: close to or equal to that arising from big bang nucleosynthesis. Population III.1 stars are defined as having their formation be independent of other stars or other astrophysical objects, so that their initial conditions are determined solely by cosmology. These stars will be the first objects to form in a given region of the universe and they are likely to play an important role in cosmic reionization and in laying the foundations for the formation and build-up of galaxies. It is possible that they are the direct or indirect progenitors of supermassive black holes.

Within the commonly accepted  $\Lambda$ CDM framework, Pop III.1 stars form within dark matter halos. Indeed, in those halos that do form stars, only one star appears to form in the center of each halo (Abel et al. 2002; Bromm, Coppi, & Larson 2002).

One of the most theoretically well-motivated cold dark matter candidates is a Weakly-Interacting Massive Particle (WIMP). Supersymmetric theories with R-parity naturally provide a stable dark matter candidate which could compose all or part of the dark matter in the Universe.

It has been pointed out that, if dark matter consists of a WIMP such as the supersymmetric neutralino, the energy released by the annihilation of these particles could influence early structure formation, star formation and protostellar evolution (Ripamonti, Mapelli & Ferrara 2007; Ascasibar 2007; Spolyar, Freese, & Gondolo 2008; Iocco 2008; Freese, Spolyar & Aguirre 2008; Freese et al. 2008b,c). The effects on stellar evolution at fixed mass have also been investigated (Taoso et al. 2008; Yoon, Iocco & Akiyama 2008). Spolyar et al. (2008) show that, for the adiabatically-contracted Navarro, Frenk & White (1996) (NFW) dark matter density profiles they considered, dark matter heating can overwhelm gas cooling in the innermost region of a star-forming minihalo, and they propose that this can then lead to a dark matter powered star.

In this paper we revisit the scenario investigated by Spolyar et al. (2008). In §2 we derive an analytic expression for the dark matter heating rate, including a simplified treatment of radiative transport. In §3 we present our results of the assessment of the importance of WIMP annihilation heating for several halos formed in numerical simulations of cosmic structure formation (O’Shea & Norman 2007). We describe the dark matter density structure in §3.1 and the properties of the baryons in §3.2. We compare the WIMP annihilation heating rates and the baryonic cooling rates and discuss the equilibrium structure of dark matter powered protostars in §3.3. We discuss the implications for subsequent protostellar evolution in §3.4. We conclude in §4.

## 2. ANALYTIC PRESCRIPTION FOR WIMP ANNIHILATION HEATING

Let us consider WIMPs with a mass  $m_\chi$ . Let  $\langle \sigma_a v \rangle$  be the WIMP annihilation cross section times the relative velocity, averaged over the momentum distribution of the WIMPs. For numerical evaluations in this paper we will assume it has a value  $3 \times 10^{-26} \text{ cm}^3 \text{ s}^{-1}$  (e.g. Jungman, Kamionkowski & Griest 1996). The number of photons produced by WIMP annihilation per unit volume, per unit time and per unit energy, at the point  $r'$  is (Hall & Gondolo 2006; Bergström, Ullio & Buckley 2006):

$$\frac{d\mathcal{N}_\gamma}{dE_\gamma} = \frac{\rho_\chi^2(r') \langle \sigma_a v \rangle}{2m_\chi^2} \frac{dN_\gamma}{dE_\gamma}, \quad (1)$$

where  $\rho_\chi(r')$  is the WIMP density at  $r'$  and  $dN_\gamma/dE_\gamma$  is the number of photons produced per unit energy per annihilation.

Let us consider electron scattering at a location  $r$ , by photons produced at the location  $r'$ . Some of the photons produced at  $r'$  will scatter off electrons before reaching the location  $r$ . The number of photons reaching  $r$  without scattering is smaller than the number produced at  $r'$  by the factor  $S$ :

$$S(r', r, E, \theta) = \begin{cases} \exp \left[ -\sigma_{e-\gamma}(E_\gamma) \int_0^{s_+} ds n_e(s) \right] & \text{when } r' < r \\ \exp \left[ -\sigma_{e-\gamma}(E_\gamma) \int_0^{s_-} ds n_e(s) \right] \\ \times \left( 1 + \exp \left[ -\sigma_{e-\gamma}(E_\gamma) \int_{s_-}^{s_+} ds n_e(s) \right] \right) & \text{when } r' > r \end{cases} \quad (2)$$

where  $s_\pm = r' \cos \theta \pm \sqrt{r^2 - r'^2 \sin^2 \theta}$  and  $\sigma_{e-\gamma}$  is the cross section. Eq. 2 takes account of the fact that photons can pass through the sphere  $r = \text{constant}$  twice when  $r' > r$ . We note that  $S$  is a function of the angle  $\theta$  between the path of the photon and the line joining  $r'$  with the center of the spherical cloud.

Consider photons that travel from  $r'$  to  $r$ . The number of scattering events per unit energy, per unit time, per unit volume at  $r$ , along the path  $\theta$  is then

$$\frac{d\mathcal{N}_s}{dE_\gamma} = \frac{\langle \sigma_a v \rangle}{2m_\chi^2} \frac{dN_\gamma}{dE_\gamma} \int dr' r'^2 \rho_\chi^2(r') S(r', r, E, \theta) \frac{n_e(r) \sigma_{e-\gamma}(E_\gamma) \delta s(r', r, \theta)}{r^2 \delta r}, \quad (3)$$

where  $\delta s$  is the distance between  $r$  and  $r + \delta r$ , along the path of the photon:

$$\delta s = \frac{\delta r}{\sqrt{1 - \frac{r'^2}{r^2} \sin^2 \theta}}. \quad (4)$$

Since all angles  $\theta$  are equally probable, we compute the angle averaged quantity  $\langle \bar{S} \rangle$ :

$$\langle \bar{S}(r', r, E) \rangle = \frac{1}{2} \int_0^{\theta_{max}} d\theta \sin \theta \frac{S(r', r, E, \theta)}{\sqrt{1 - \frac{r'^2}{r^2} \sin^2 \theta}}. \quad (5)$$

$\theta_{max} = \pi$  when  $r' < r$  and  $\theta_{max} = \sin^{-1}(r/r')$  when  $r' > r$ .

In the limit that the wavelength of the incident radiation is much smaller than the Bohr radius, we may assume that the radiation sees a gas of electrons and protons, rather than bound atoms. With this approximation, the scattering cross section  $\sigma_{e-\gamma}(E_\gamma)$  is given by the Klein-Nishina formula (e.g. Peskin & Schroeder 1995)

$$\sigma_{e-\gamma}(y) = \sigma_T f_\sigma(y), \quad (6)$$

where  $\sigma_T$  is the Thomson cross section for electrons (proton scattering is less important owing to the large mass).  $f_\sigma$  is given by

$$f_\sigma(y) = \frac{3}{8} \left[ \frac{2(1+y)}{(1+2y)^2} + \frac{\ln(1+2y)}{y} - \frac{2}{1+2y} + \frac{2(1+y)^2}{y^2(1+2y)} - \frac{2(1+y)\ln(1+2y)}{y^3} + \frac{2}{y^2} \right], \quad (7)$$

where  $y = E_\gamma/m_e$ .  $E_{\text{abs}}$  is the average energy transferred to an electron in a scattering event:

$$E_{\text{abs}} = m_\chi f_E(E_\gamma), \quad (8)$$

where

$$f_E = \frac{E_\gamma}{m_\chi} + \frac{m_e}{m_\chi} - \frac{m_e}{2m_\chi} \ln \left( 1 + \frac{2E_\gamma}{m_e} \right). \quad (9)$$

Let us make the assumption that the energetic electrons (after scattering) remain in the gas cloud and serve to heat up the cloud. As long as low energy photons do not contribute significantly to the heating rate, we may maintain our approximation  $E_\gamma \gg 13.6 \text{ eV}$ , while performing the energy integral:

$$H(r) = \frac{\langle \sigma_a v \rangle n_e(r) \sigma_T}{2m_\chi r^2} \int_0^{m_\chi} dE_\gamma f_E(E_\gamma) f_\sigma(E_\gamma) \frac{dN_\gamma}{dE_\gamma}(E_\gamma) \int_0^r dr' r'^2 \rho_\chi^2(r') \langle \bar{S}(E_\gamma, r', r) \rangle. \quad (10)$$

$H(r)$  gives the heating rate (energy per unit volume per unit time) at the point  $r$  due to primary photons, under the approximate assumption that all the primary photon energy is transferred to the gas at the location of the first collision. Note, we are not solving the full radiation transfer problem in determining  $H(r)$ , especially the distributed heating effects of secondary pair and photon production, and so our treatment is still an approximate one.

2.1. *The  $\langle S(r, r', E) \rangle$  function.*

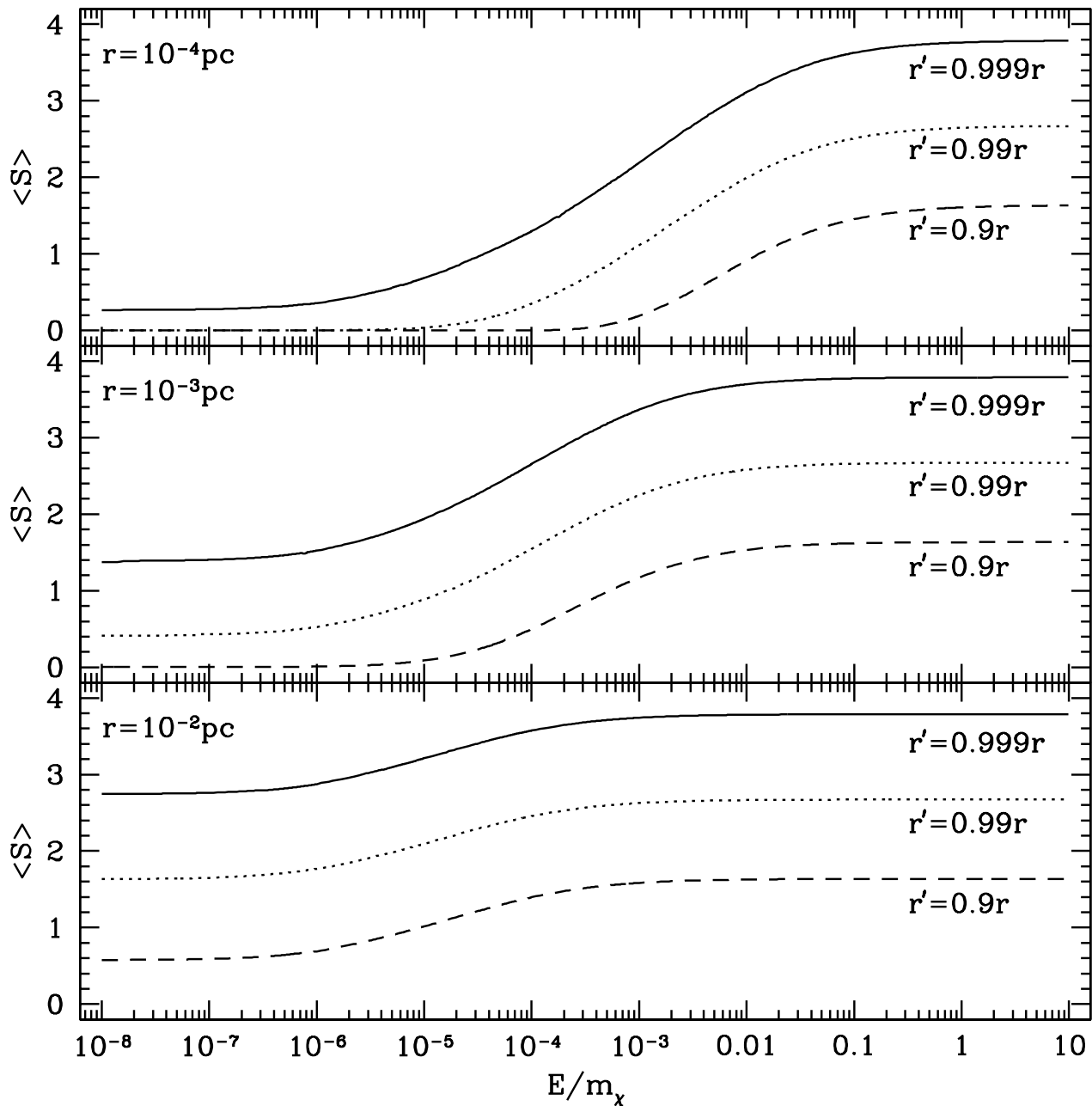


FIG. 1.— The  $\langle S(r, r', E) \rangle$  function for  $m_\chi = 100$  GeV.  $S$  is small for small energies because of the larger scattering cross section.  $S$  is also small when the point  $r'$  is far from  $r$ . These effects are more pronounced for small  $r$  (high gas density).

In order to compute the heating rate at a point  $r$  using Eq. 10, we need to consider dark matter in a finite volume around  $r$ . The size of this volume is determined by the function  $\langle S(r, r', E) \rangle$ . When this volume is small compared to the size of the halo, one may expect most of the energy released by dark matter annihilation to be absorbed by the gas cloud. Figure 1 shows  $\langle S \rangle$  for the cases  $r = 10^{-4}, 10^{-3}$  and  $10^{-2}$  pc. The three curves in each panel correspond to values of

$r' = 0.999r$ ,  $r' = 0.99r$  and  $r' = 0.9r$ . As expected,  $S$  is largest when  $r'$  is close to  $r$ . More energetic photons penetrate farther through the gas owing to the smaller scattering cross section.

### 3. NUMERICAL RESULTS FOR WIMP ANNIHILATION HEATING AND BARYONIC COOLING RATES

We analyzed the structure of the three highest resolution star-forming minihalos in the numerical simulations presented by O’Shea & Norman (2007). We will refer to these simulation runs as A, B, C. These simulations were performed using the Enzo code, which is an adaptive mesh refinement (AMR) cosmology code developed by G. Bryan and others (e.g. O’Shea et al. 2004). The code couples an N-body particle mesh (PM) solver (Efsthathiou et al. 1985; Hockney & Eastwood 1998) with Eulerian AMR. All simulations were initialized at  $z = 99$  assuming a concordance cosmological model with  $\Omega_m = 0.3$ ,  $\Omega_b = 0.04$ ,  $\Omega_{\text{CDM}} = 0.26$ ,  $\Omega_\Lambda = 0.7$ ,  $h = 0.7$ ,  $\sigma_8 = 0.9$  and an Eisenstein & Hu (1999) power spectrum with a spectral index  $n = 1$ . Each of the three star-forming minihalos was formed in a separate simulation with a different random seeding of the initial conditions and a box size of  $0.3h^{-1}$  Mpc (comoving). The most massive halo to form in each simulation, at  $z = 15$  (typically with a mass  $\sim 10^6 M_\odot$ ) was found using a dark matter only computation. The initial conditions were then regenerated with both dark matter and baryons such that the Lagrangian volume in which the halo formed was resolved at much higher spatial and mass resolution.

#### 3.1. Dark Matter Density Structure and Heating Rate

The minimum dark matter particle mass in the simulations was  $1.81h^{-1} M_\odot \rightarrow 2.59 M_\odot$ . To avoid effects due to the finite size of the dark matter particles, the dark matter density was smoothed on a comoving scale of 0.5 pc, i.e. a proper scale of  $\sim 0.025$  pc at  $z \sim 20$ . Note that the gravitational forces due to the baryonic core of the minihalo are not smoothed, since there is high spatial resolution in this region. At their final timestep, all simulations had more than 100 dark matter particles inside a proper scale of 1 pc.

The dark matter density profile is not resolved in the very central regions of the halo where WIMP annihilation heating may be important. Thus the results of these simulations are used as a guide for two extrapolation methods (DM fits #1 and #2) to estimate the dark matter density on scales of  $\sim 10^{-5} - 10^{-4}$  pc. We fit power laws of the form

$$\rho_\chi = A_\chi \left( \frac{r}{\text{pc}} \right)^{-\alpha_\chi} \quad (11)$$

to the radial dark matter density profiles, evaluated over particular ranges in radius. DM fit #1, shown in Fig. 2, uses only data points from the central regions with more than 100 particles per bin (corresponding to scales from about 50 pc down to  $r \gtrsim 1.5$  pc). We find  $\alpha_\chi = 1.35, 1.24, 1.65$  and  $A_\chi = 1674, 1696, 2732 \text{ GeV cm}^{-3}$  for simulations A, B, C, respectively. Note that simulation C has a significantly steeper density profile than A and B. All these density profiles are expected to underestimate the dark matter density in the inner regions of the halo, where the baryon density begins to dominate over dark matter and adiabatic contraction of the dark matter tends to steepen its profile (Blumenthal et al. 1986). Thus we consider DM fit #1 to provide a conservative lower limit to the dark matter density and thus the heating rate.

Our second extrapolation method, DM fit #2, is based on simulation data from the inner (but not the innermost,  $r < 0.025$  pc) regions (see Fig. 2). For simulation A, we have  $A_\chi = 2396 \text{ GeV cm}^{-3}$ ,  $\alpha_\chi = 1.980$  when  $r < 1$  pc (and  $A_\chi = 2409 \text{ GeV cm}^{-3}$ ,  $\alpha_\chi = 1.51$  when  $r > 1$  pc). For simulation B,  $A_\chi = 1602 \text{ GeV cm}^{-3}$ ,  $\alpha_\chi = 1.946$  when  $r < 1$  pc (and  $A_\chi = 1696 \text{ GeV cm}^{-3}$ ,  $\alpha_\chi = 1.24$  when  $r > 1$  pc). For simulation C, we have  $A_\chi = 942 \text{ GeV cm}^{-3}$ ,  $\alpha_\chi = 2.108$  when  $r < 0.1$  pc (and  $A_\chi = 2732 \text{ GeV cm}^{-3}$ ,  $\alpha_\chi = 1.645$  when  $r > 0.1$  pc). The density profiles of the inner regions show a significant steepening compared to the outer regions. This is likely to be the result of adiabatic contraction, since it occurs at a scale  $\sim 1$  pc where the density of baryons begins to dominate. We emphasize again that the simulation points on which DM fits #2 are based correspond to bins with only a small ( $< 100$ ) number of particles and must be treated with caution. We do note, however, that on the very innermost scales ( $\sim 0.01$  pc) the dark matter density profiles in the numerical simulations are even steeper than the analytic DM fits #2.

If adiabatic contraction of dark matter in the baryon-dominated potential is responsible for sculpting these profiles, one expects that the maximum steepness of the dark matter density profile will be equal to that of the baryons, which has been shown in simulations to have an approximate power law profile of  $\rho_{\text{gas}} \propto r^{-2.2}$  (see §3.2). The baryonic density profile inevitably flattens in its center, so that the power law profile is only valid inwards to some core radius,  $r_c$ . This core radius shrinks as collapse proceeds. In situations where we are interested in the global luminosity provided by WIMP annihilation in the halo (§3.3), we will assume that the dark matter density profile also exhibits this core radius, inside of which its density is also constant.

For the fiducial case, we assume a dark matter particle mass of  $m_\chi = 100 \text{ GeV}$ , which is typical for a weakly interacting particle. The photon multiplicity function  $dN_\gamma/dE_\gamma$  for the important annihilation channels is given by the form (Bergström et al. 1998; Feng et al. 2001)

$$\frac{dN_\gamma}{dx} = \frac{ae^{-bx}}{x^{1.5}}, \quad (12)$$

where  $x = E_\gamma/m_\chi$  and  $(a, b)$  are constants for the particular annihilation channel. We use the values given in Feng, Matchev & Wilczek (2001), and average over the different annihilation channels they considered to obtain  $(a = 0.9, b = 9.56)$ . We set  $\langle \sigma_a v \rangle = 3 \times 10^{-26} \text{ cm}^3 \text{ s}^{-1}$  (e.g. Jungman et al. 1996). The heating rate as expressed in equation 10 was calculated for the above density profiles and is shown in Fig. 3.

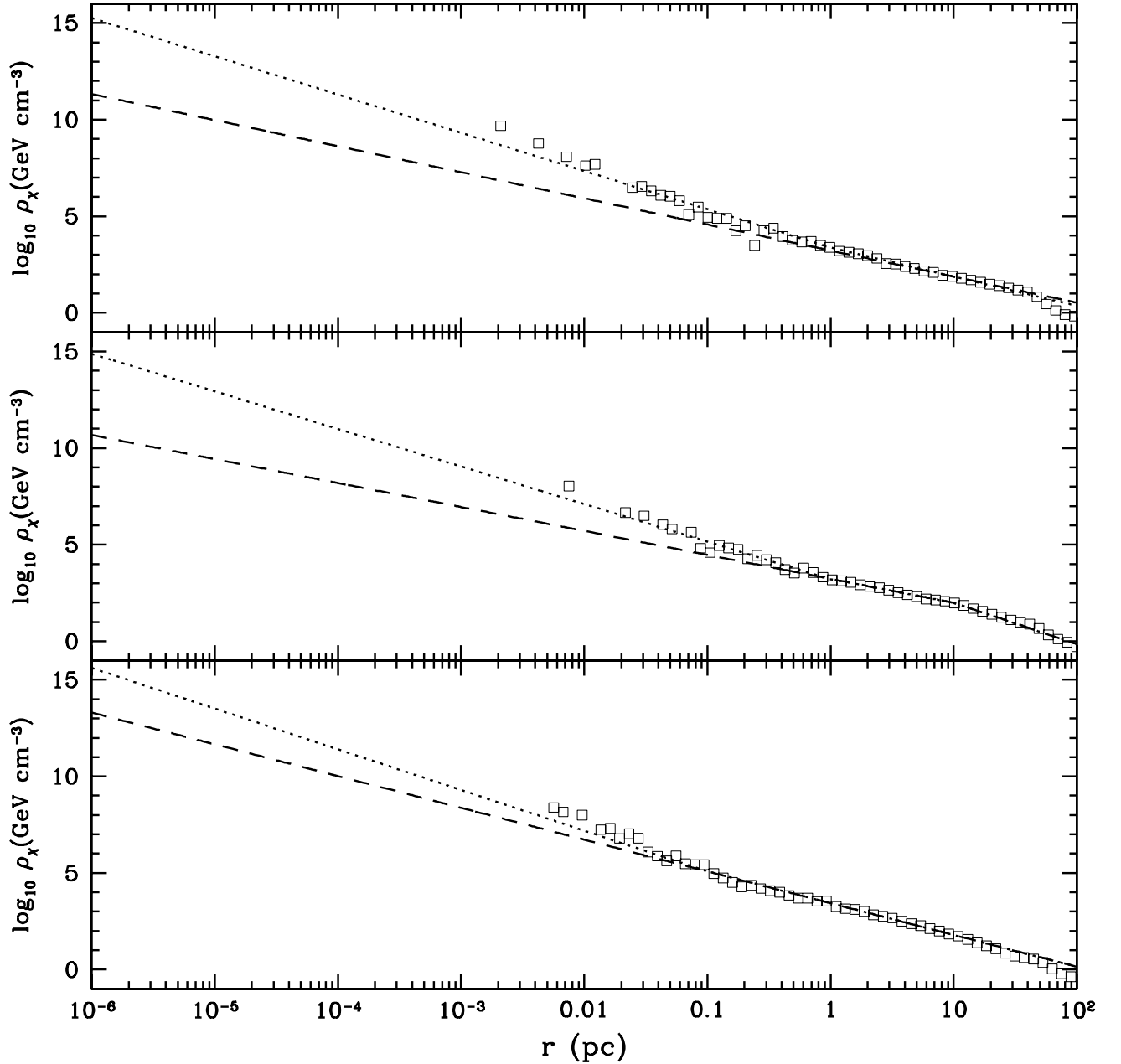


FIG. 2.— Dark matter density profiles (spherical averages) for simulations A (top), B (middle), and C (bottom) are shown with the open squares. Power law fits to the outer, well-resolved regions (fit #1) are shown with the dashed lines, while fits to the inner (but not innermost – see text), less-well-resolved, regions (fit #2) are shown with the dotted lines.

The variation of  $H(r)$  on the WIMP mass,  $m_\chi$ , is also shown in Fig. 3. We consider cases with  $m_\chi = 10$  GeV and 1 TeV, i.e. factors of 10 below and above our fiducial value. Once the simple  $m_\chi^{-1}$  dependence of  $H(r)$  (eq. 10) is accounted for, we see that remaining variations in  $H(r)$  are within about a factor of 2. These are due to the  $m_\chi$  dependencies of the photon multiplicity function, the energy integral and the  $\langle S(r, r', E) \rangle$  function.

It is also informative to compare  $H(r)$  to the energy generated by WIMP annihilation per unit volume, per unit time

$$G(r) = \frac{\rho_\chi^2(r) \langle \sigma_a v \rangle}{2m_\chi} \int_0^1 dx x \frac{dN_\gamma}{dx} \quad (13)$$

Fig. 3 compares  $G(r)$  and  $H(r)$  for Simulation A, for DM fit #2. At small distances ( $r < 100$  AU), the two curves are very similar, whereas at larger distances,  $G(r) \gg H(r)$  since not all the energy generated is absorbed. It is also interesting

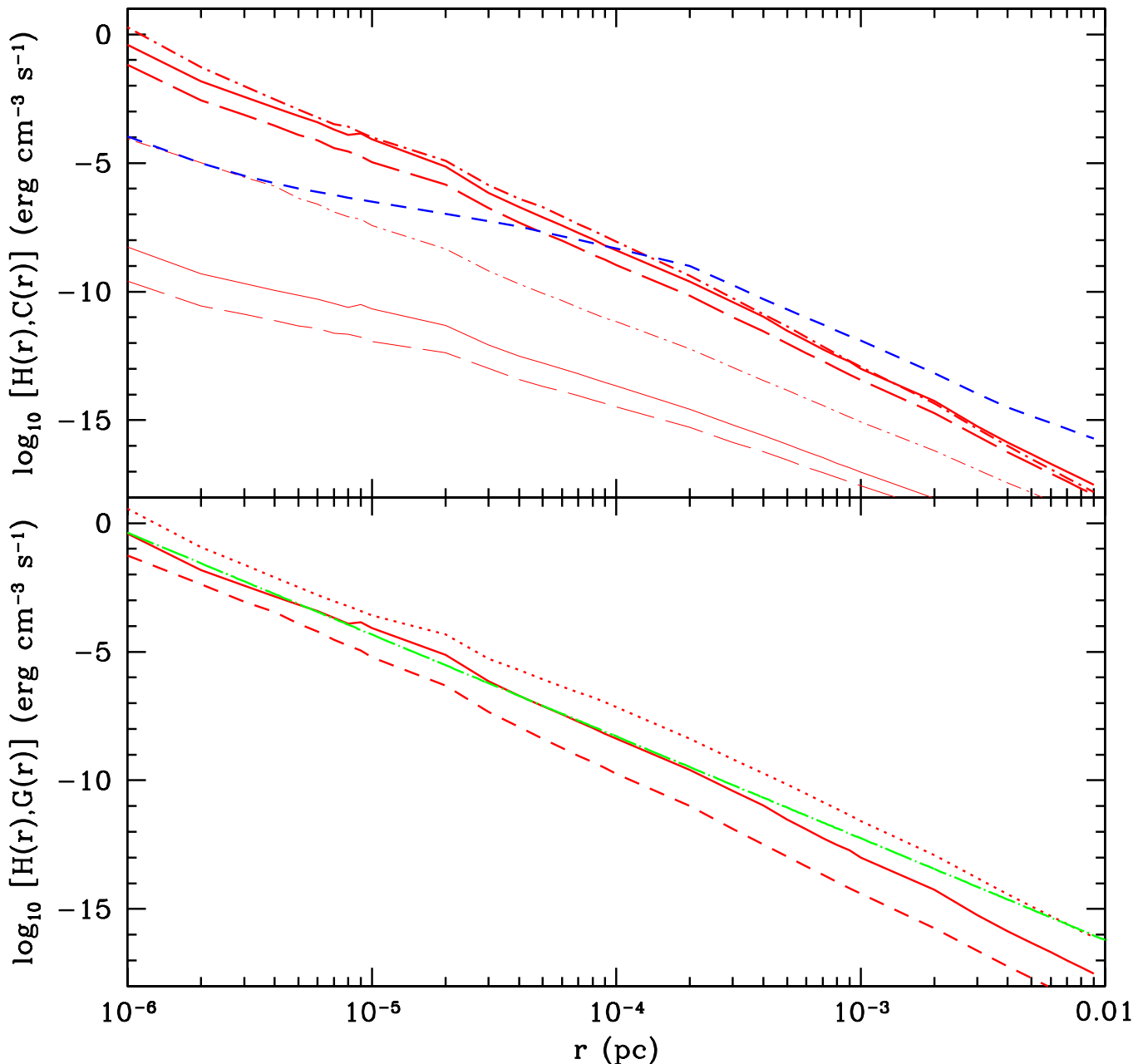


FIG. 3.— Top panel: WIMP annihilation heating rate,  $H(r)$ , for simulation A (solid lines), B (long-dashed lines) and C (dot-dashed lines) with DM fit #1 (lower, thin lines) and DM fit #2 (upper, thick lines). All these models assume  $m_\chi = 100$  GeV. The cooling rate,  $C(r)$ , is shown by the dashed line (see §3.2). Bottom panel: Variation of  $H(r)$  with WIMP mass for simulation A, DM profile #2. WIMP masses  $m_\chi = 10, 100$  and  $1000$  GeV are shown by the dotted, solid, and dashed lines, respectively. The dot-long-dashed line shows the WIMP annihilation energy generation rate,  $G(r)$ , for  $m_\chi = 100$  GeV (it is to be compared with the solid line). At large radii,  $H(r)$  becomes much smaller than  $G(r)$ , since not all the energy generated is absorbed.

to note that  $H(r)$  can exceed  $G(r)$  at high densities, since unlike  $G(r)$ ,  $H(r)$  is not a strictly local function of  $r$ .

### 3.2. Baryon Density, Temperature, $H_2$ Fraction and Cooling Rate

In the numerical simulations of O’Shea & Norman (2007), collapse of baryons was followed with adaptive mesh refinement to much higher spatial resolution than the dark matter. Spatial scales down to  $115h^{-1} \rightarrow 164$  AU (comoving), i.e. about 10 AU (proper), were resolved (see Fig. 4). However, in many cases we consider, knowledge of the gas properties is required on even smaller scales. Thus we utilize the results of the even higher resolution smooth particle hydrodynamics (SPH) simulations of Yoshida et al. (2006), which were carried out for a single minihalo in which the collapse was followed

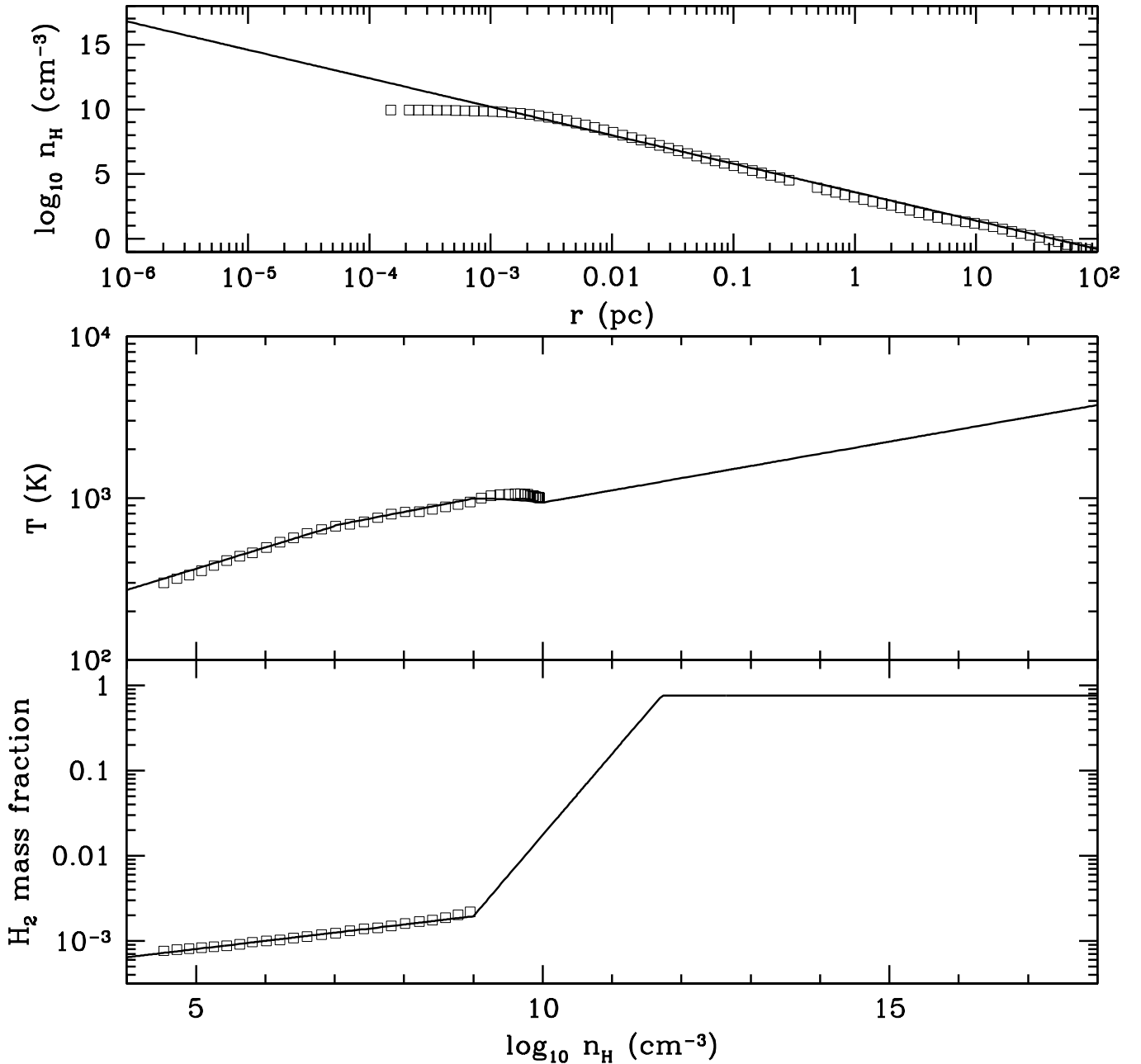


FIG. 4.— Top panel: radially-averaged H number density,  $n_{\text{H}}$ , for simulation A (open squares). The solid line shows a power law  $n_{\text{H}} \propto r^{-2.2}$ , normalized from the simulations of Yoshida et al. (2006) to have  $\log_{10}(n_{\text{H}}/\text{cm}^{-3}) = 13.15$  at  $r = 10 \text{ AU} = 4.88 \times 10^{-5} \text{ pc}$ . Middle panel: radially-averaged temperature,  $T$ , versus radially-averaged H number density,  $n_{\text{H}}$  for simulation A (open squares). The solid line shows the analytic fits estimated from the results of Yoshida et al. (2006). Bottom panel: radially-averaged  $\text{H}_2$  mass fraction versus radially-averaged  $n_{\text{H}}$  for simulation A (open squares). The solid line shows the analytic fits estimated from the results of Yoshida et al. (2006).

to higher densities. The structure of baryonic core is controlled mostly by the microphysics of  $\text{H}_2$  cooling, in which case one expects a fairly universal profile of density, temperature and chemical composition.

For the Hydrogen number density,  $n_{\text{H}} = 0.76\rho_{\text{gas}}/m_p$ , we use the analytic fit

$$n_{\text{H}} = 1.41 \times 10^{13} \left( \frac{r}{10 \text{ AU}} \right)^{-2.2} \text{ cm}^{-3}, \quad (14)$$

which is based on conditions at 10 AU in the simulation of Yoshida et al. (2006). Figure 4 shows this fit is also a good description of the gas in the simulations of O’Shea & Norman (2007) at  $r \geq 200 \text{ AU}$ .

The temperature profile (as a function of density) at densities  $n_{\text{H}} > 10^9 \text{ cm}^{-3}$  was fit with an analytic function based

on the results of Yoshida et al. (2006). For lower densities, our simulations A, B and C are reliable. We use the fitting functions (see Fig. 4):  $T = 165.5(n_{\text{H}}/\text{cm}^{-3})^{0.0754} \text{ K}$  for densities  $n_{\text{H}} > 10^{10} \text{ cm}^{-3}$ ;  $\log(T/\text{K}) = 3 - 0.025 \log^2(n_{\text{H}}/10^9 \text{ cm}^{-3})$  for densities  $10^9 \text{ cm}^{-3} < n_{\text{H}} < 10^{10} \text{ cm}^{-3}$ ;  $T = 178(n_{\text{H}}/\text{cm}^{-3})^{0.083} \text{ K}$  for densities  $10^7 \text{ cm}^{-3} < n_{\text{H}} < 10^9 \text{ cm}^{-3}$ ; and  $T = 80.5(n_{\text{H}}/\text{cm}^{-3})^{0.1315} \text{ K}$  for densities  $n_{\text{H}} < 10^7 \text{ cm}^{-3}$ .

The molecular hydrogen mass fraction  $f_{\text{mol}}$  is also fit from the results of the simulations of O’Shea & Norman (2007) and Yoshida et al. (2006). We use the fitting functions (see Fig. 4):  $f_{\text{mol}} = 5 \times 10^{-12}(n_{\text{H}}/\text{cm}^{-3})^{0.954}$  for densities  $n_{\text{H}} > 10^9 \text{ cm}^{-3}$  (Yoshida et al. 2006) and  $f_{\text{mol}} = 2.64 \times 10^{-4}(n_{\text{H}}/\text{cm}^{-3})^{0.0963}$  for densities  $n_{\text{H}} < 10^9 \text{ cm}^{-3}$  (O’Shea & Norman 2007).

We use the analytic results of Hollenbach & McKee (1979) to implement rotational and vibrational  $\text{H}_2$  cooling. Collision-induced emission (CIE) cooling follows the fit published in Yoshida et al. (2006). We also account for the loss of cooling efficiency due to the gas becoming optically thick. The opacity of the gas to cooling radiation was measured from the results of Yoshida et al. (2006). The cooling efficiency,  $\eta$ , follows the fitting function:  $\eta = 9.4 \times 10^5(n_{\text{H}}/\text{cm}^{-3})^{-0.548}$  for densities  $n_{\text{H}} > 10^{13} \text{ cm}^{-3}$ ;  $\eta = 900(n_{\text{H}}/\text{cm}^{-3})^{-0.316}$  for densities  $10^{11} \text{ cm}^{-3} < n_{\text{H}} < 10^{13} \text{ cm}^{-3}$ ;  $\eta = 1.7 \times 10^5(n_{\text{H}}/\text{cm}^{-3})^{-0.523}$  for densities  $10^{10} \text{ cm}^{-3} < n_{\text{H}} < 10^{11} \text{ cm}^{-3}$ ; and  $\eta = 1$  for lower densities.

The cooling rate,  $C(r)$ , is shown in Fig. 3 for simulation A. The results for simulations B and C are very similar.

### 3.3. Comparison of Heating and Cooling Rates and the Equilibrium Structure

Figure 5 shows the radial profiles of the ratio of the heating rate caused by WIMP annihilation to the gas cooling rate,  $H(r)/C(r)$ , for simulations A, B, C and dark matter density fits #1 and #2, assuming  $m_{\chi} = 100 \text{ GeV}$ . For simulation A, the dependence on  $m_{\chi}$  is also illustrated using  $m_{\chi} = 10 \text{ GeV}$  and  $1000 \text{ GeV}$ . Results are also shown as a function of  $n_{\text{H}}$ , using equation 14 to derive the density at a given radius.

For the conservative, relatively shallow dark matter density profiles (fit #1) of simulation A and B and for a fiducial WIMP mass of  $100 \text{ GeV}$ , the heating rate is never larger than  $\sim 10^{-4}$  of the cooling rate for densities up to  $n_{\text{H}} = 10^{17} \text{ cm}^{-3}$ . In this situation we expect that the star formation process from these gas cores, in particular the protostellar structure and accretion rate (e.g. Tan & McKee 2004) would be unaffected by dark matter annihilation heating. The expected mass of the stars forming from these halos is then  $\sim 100 - 200 M_{\odot}$ , set by ionizing feedback, especially disk photoevaporation, on the protostellar accretion flow (McKee & Tan 2008).

The case of DM fit #1 for simulation C is somewhat steeper ( $\alpha_{\chi} = 1.65$ ) than for simulations A and B ( $\alpha_{\chi} \simeq 1.3$ ), and this leads to the heating rate becoming comparable to the cooling rate at  $n_{\text{H}} \gtrsim 10^{15} \text{ cm}^{-3}$ . This trend is continued for the steeper density profiles of DM fit #2, all of which have a central region where WIMP annihilation heating dominates over cooling, typically for  $r \lesssim 10^{-4} \text{ pc}$ , i.e.  $20 \text{ AU}$ , and  $n_{\text{H}} \gtrsim 10^{12} \text{ cm}^{-3}$ . One important factor setting this density scale is drop in the cooling efficiency of the gas (Yoshida et al. 2006, their Fig. 4) because of the increasing opacity of the gas.

These results are broadly consistent with the those of Spolyar et al. (2008), showing that the properties of the dark matter heating dominated core are relatively insensitive to the details of radiative transport of the WIMP annihilation heating that we have included, and that their analytic model for the dark matter density distribution is similar to our DM fit #2 to simulated minihalos (see also Freese et al. 2008b).

The expected consequence of a central core where dark matter heating of the gas dominates its radiative cooling is a halt to the collapse. This process would then set the core radius,  $r_c$ , for both the dark matter and baryon density distributions. To evaluate this core radius and the total luminosity of the equilibrium structure, we now consider the enclosed luminosity profile,  $L(r)$ , of the halos, defined for WIMP annihilation heating as

$$L_{\chi}(r) = 4\pi \int_0^r dr' r'^2 H(r'), \quad (15)$$

and for baryonic cooling as

$$L_{\text{gas}}(r) = 4\pi \int_0^r dr' r'^2 C(r'). \quad (16)$$

The luminosity due to WIMP annihilation will be dominated by the central part of the halo for  $\alpha_{\chi} > 1.5$  (eq. 13), which is the case for all DM fits #2. We solve for the core radius,  $r_c$ , for each simulation via the condition  $L_{\chi}(r \rightarrow \infty) = L_{\text{gas}}(r \rightarrow \infty)$ , i.e.

$$\frac{4\pi r_c^3}{3} H(r_c) + 4\pi \int_{r_c}^{\infty} dr r^2 H(r) = \frac{4\pi r_c^3}{3} C(r_c) + 4\pi \int_{r_c}^{\infty} dr r^2 C(r). \quad (17)$$

This is an equilibrium condition in the sense that the energy generation rate by dark matter annihilation heating balances that radiated away by the baryons. Note that for the profiles analyzed here, both heating and cooling luminosities are dominated by the central regions, i.e. the integrals converge to a finite value as  $r \rightarrow \infty$ . Note also that local heating will dominate local cooling in an inner region that is somewhat larger than  $r_c$ , and cooling will dominate heating outside of this region.

Figure 6 shows the luminosity profiles for DM fit #2 for simulations A, B and C with  $m_{\chi} = 100 \text{ GeV}$ , and for simulation A with  $m_{\chi} = 10 \text{ GeV}$  and  $1 \text{ TeV}$ . Also shown is  $L_{\text{gas}}$  for the fiducial model. With  $m_{\chi} = 100 \text{ GeV}$ , the core radii for simulations A, B, C are  $r_c = 7.4, 2.2, 19 \text{ AU}$ , respectively, and  $L_{\chi}(r \rightarrow \infty) = 1460, 1540, 781 L_{\odot}$ , respectively. The dark matter density in these cores are  $\rho_{\chi,c} = 1.5 \times 10^{12}, 7.5 \times 10^{12}, 3.0 \times 10^{11} \text{ GeV cm}^{-3}$ , respectively. For simulation A

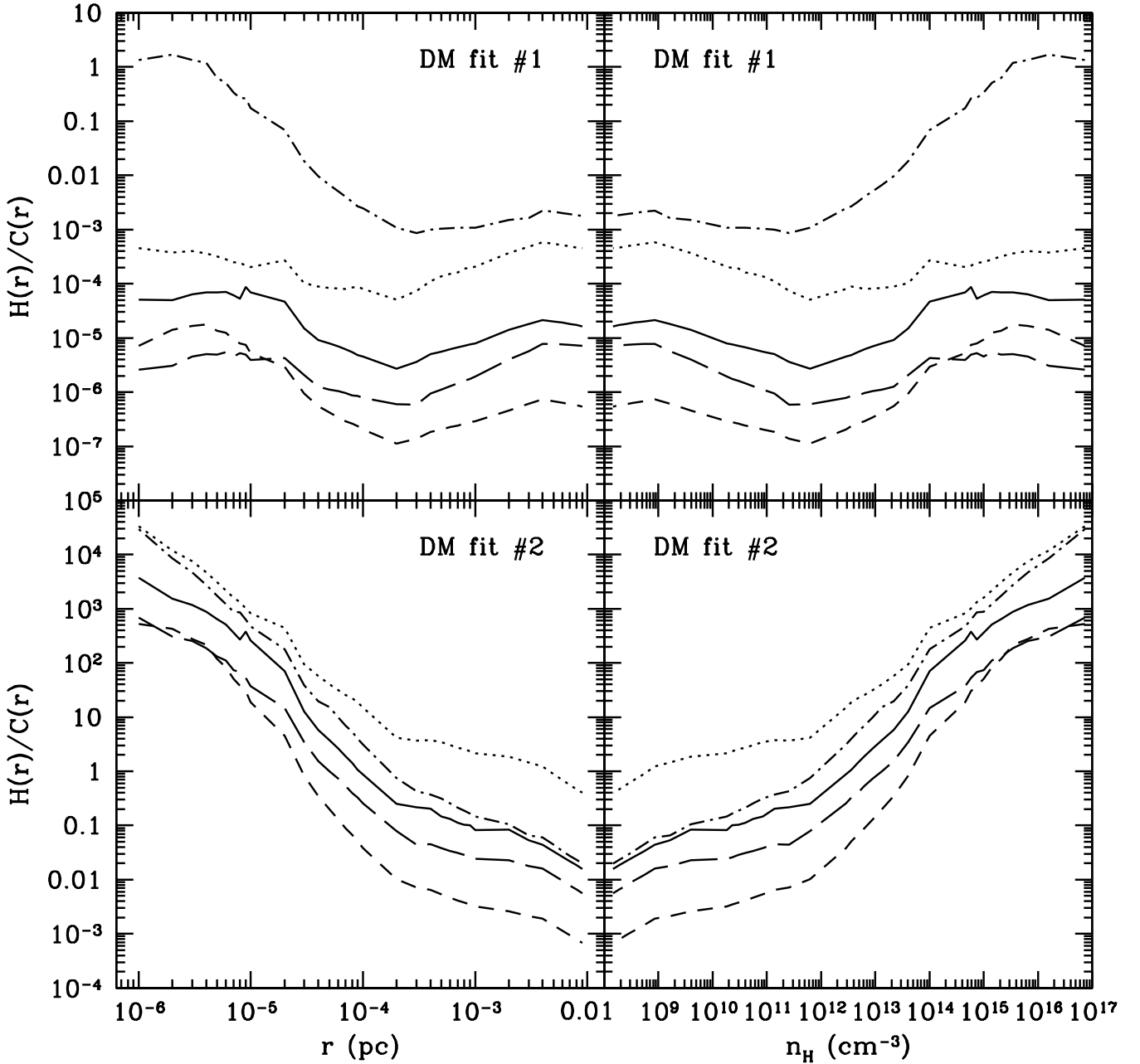


FIG. 5.— Ratio of dark matter annihilation heating rate,  $H(r)$ , to baryonic cooling rate,  $C(r)$ , for dark matter density fits #1 (top panels) and #2 (bottom panels) for simulations A (solid lines), B (long-dashed lines), C (dot-dashed lines) for  $m_\chi = 100$  GeV. Results for simulation A with  $m_\chi = 10$  GeV (dotted lines) and  $m_\chi = 1$  TeV (dashed lines) are also shown.

with  $m_\chi = 10$  GeV and 1 TeV, we find  $r_c = 37, 0.93$  AU, respectively,  $L_\chi(r \rightarrow \infty) = 960, 1510 L_\odot$ , respectively, and  $\rho_{\chi,c} = 6.2 \times 10^{10}, 9.2 \times 10^{13}$  GeV cm $^{-3}$ , respectively.

The constancy of these total luminosities is set by the baryonic cooling luminosity, which is dominated by the region from  $\sim 10$  AU to  $\sim 100$  AU, and is independent of the much smaller core radius, which adjusts itself so as to provide enough WIMP annihilation luminosity to match that radiated away by the baryons.

We note our solution has made the approximation that the baryonic properties used to estimate  $L_{\text{gas}}$  do not include the effects of WIMP annihilation heating. This effect would lead to hotter temperatures and more efficient cooling, so that the actual equilibrium structure would be somewhat smaller and denser.

Energy transport from the hotter inner part of the halo to the outer cooler part, either via convection or radiation, would be needed to set up a hydrodynamic equilibrium: i.e. a dark matter powered (proto)star. The size of this star

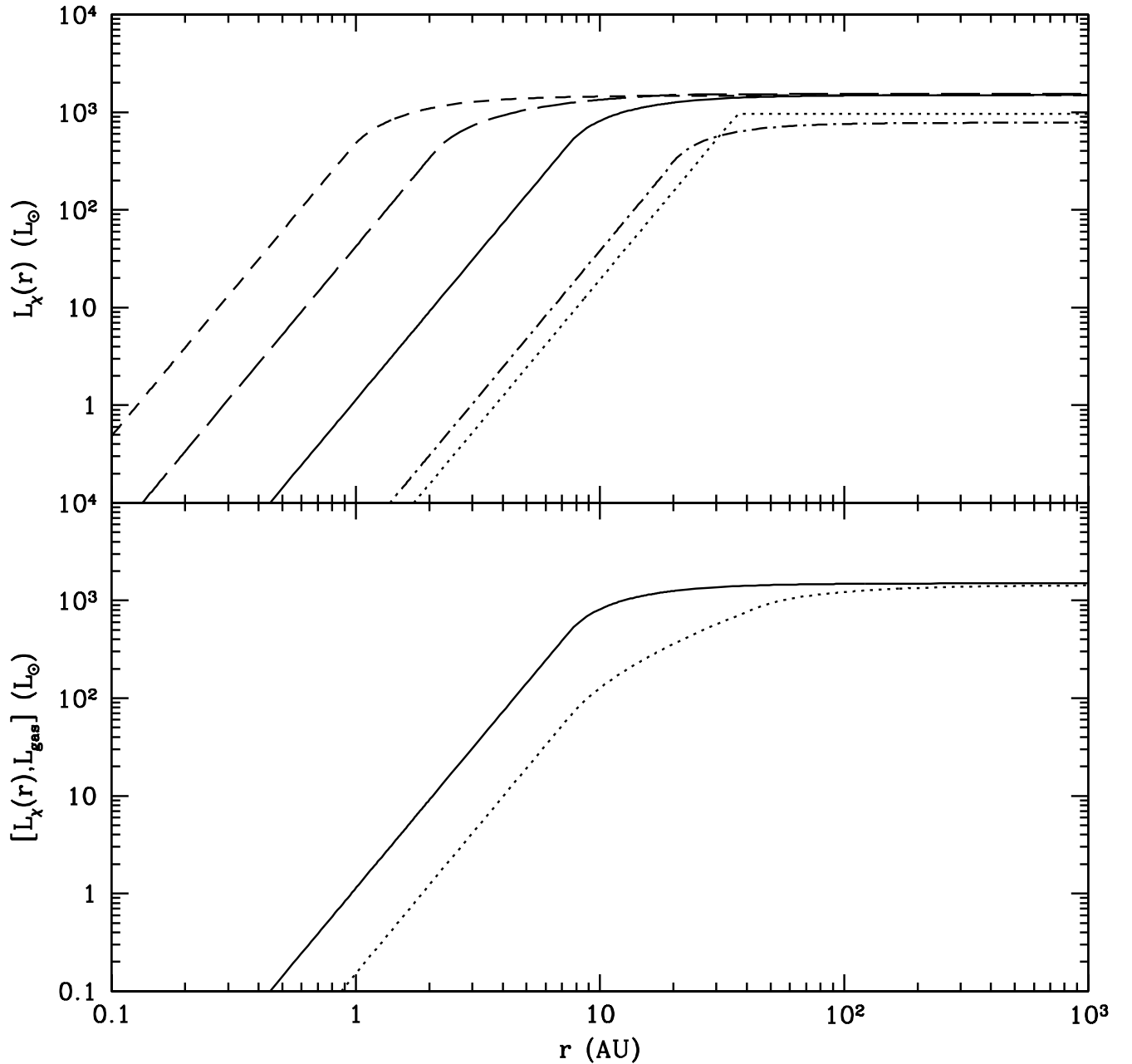


FIG. 6.— Enclosed luminosity generated from the heating due to dark matter annihilation,  $L_\chi(r)$ , for the equilibrium halo configurations (see text). The top panel shows  $L_\chi(r)$  for simulations A (solid line), B (long-dashed line), C (dot-dashed line), assuming  $m_\chi = 100$  GeV and dark matter density fit #2. The same model for simulation A, but with  $m_\chi = 10$  GeV is shown with the dotted line and with  $m_\chi = 1$  TeV is shown with the dashed line. The bottom panel compares  $L_\chi(r)$  for simulation A, dark matter density fit #2 and  $m_\chi = 100$  GeV (solid line) with the baryonic cooling luminosity,  $L_{\text{gas}}(r)$ , (dotted line) for the same halo.

would be set by the  $\tau = 1$  surface, beyond which the energy flux from the interior is free to escape. The results of Yoshida et al. (2006) imply that the cooling efficiency has dropped to 0.1 by the time  $n_{\text{H}} = 10^{12} \text{ cm}^{-3}$ , corresponding to about 30 AU. This is an approximate upper limit to the initial size of the protostar, since the actual gas temperature will be somewhat hotter and a larger fraction of the radiated energy would be in the continuum (as opposed to line radiation).

### 3.4. Subsequent Evolution of the Dark Matter Powered Protostar

Since there is a large mass reservoir at large  $r$  that is undergoing cooling, baryons will continue to accrete to the central protostar, deepening the gravitational potential and thus causing more dark matter to be concentrated here also. For

simulation A, DM fit#2 and  $m_\chi = 100$  GeV with  $r_c = 7.4$  AU, the mass inside  $r_c$  is  $0.17 M_\odot$ , and the accretion rate is close to  $0.1 M_\odot \text{yr}^{-1}$  with infall speeds of about  $4 \text{ km s}^{-1}$  (Yoshida et al. 2006), which are mildly supersonic. As the central mass grows, the infall is expected to become more supersonic, i.e. closer to the free fall speed of the central protostellar mass at its surface.

The detailed evolution of this dark matter powered protostar is beyond the scope of this paper. Freese et al. (2008c) have considered the protostellar structure of such stars, but starting from a more evolved stage when  $m_* = 3 M_\odot$  and for  $\dot{m}_* = 2 \times 10^{-3} M_\odot \text{yr}^{-1}$ . After 4,500 yr of accretion this initial structure has grown in mass to  $12 M_\odot$  and has a radius of 2.8 AU and a luminosity of  $1.1 \times 10^5 L_\odot$  (ignoring accretion luminosity). The dark matter in the star is assumed to increase via adiabatic contraction of the surrounding halo and enough luminosity is provided by dark matter annihilation to support stars of at least  $1000 M_\odot$ , for which  $L_* = 4 \times 10^6 L_\odot$ . Being much larger and cooler than protostars on the zero age main sequence (ZAMS), these dark matter powered protostars are expected to have relatively weak radiative feedback on their accretion envelopes and thus may be able to attain very high masses.

An alternative possibility is that the baryonic mass of the star grows more rapidly than the enclosed dark matter mass and that this more massive star is unable to be supported by WIMP annihilation luminosity. The star contracts and reaches central densities and temperatures at which nuclear fusion of H starts. Note that fiducial models of Population III.1 protostars (e.g. Omukai & Palla 2003; Tan & McKee 2004) do not expect contraction to the main sequence until  $m_* \simeq 100 M_\odot$ , i.e. when the Kelvin-Helmholz time becomes less than the accretion growth time. The critical feedback process, disk photoevaporation, theorized to limit the masses of Pop III.1 stars is expected to truncate protostellar growth along the ZAMS at about  $140 M_\odot$ , depending on the accretion rate (McKee & Tan 2008). Thus if WIMP annihilation were able to support the protostar only up to  $\sim 100 M_\odot$ , there would be only modest implications for the initial mass function of the first stars.

Understanding the accumulation of dark matter by the protostar is of critical importance for deciding between these two scenarios. There are processes and effects that can cause inefficient adiabatic contraction of the dark matter halo in response to protostellar accretion. Rapid free-fall collapse of the baryons joining the star-disk system is expected after the expansion wave moves out. Standard analytic analyses of adiabatic contraction typically assume very slow changes in the baryonic potential (e.g. Blumenthal et al. 1986). For rapid collapse, one expects a delayed response of the dark matter, and during this time  $m_{*DM}/m_*$  will have decreased.

Another effect is excitation of the dark matter velocity dispersion by scattering with baryonic density fluctuations. These will probably occur most strongly in the accretion disk around the protostar, since such fluctuations are required for angular momentum transport, and, if not initially present, will inevitably develop via gravitational instability as the disk mass grows (Tan & Blackman 2004). For accretion from a core with a given density and angular momentum, the disk size can be described via (Tan & McKee 2004):

$$r_d = 3.44 \left( \frac{f_{\text{Kep}}}{0.5} \right)^2 \left( \frac{m_{*d}}{M_\odot} \right)^{9/7} K'^{-10/7} \text{ AU}, \quad (18)$$

where  $f_{\text{Kep}}$  is the ratio of the rotational to Keplerian velocities of the gas at the sonic point of the infall and has a fiducial value of 0.5 in the simulations of Abel et al. (2002),  $m_{*d}$  is the mass of central protostar and its disk (we typically assume a disk mass that is one third of the protostellar mass), and  $K'$  is the normalized entropy parameter (related to the density of the core at the time of protostar formation: a denser core has a larger value of  $K'$ ), with fiducial value of 1.0. We see that the expected disk sizes when the central mass is 1, 10, 100  $M_\odot$  are 3.4, 66, 1300 AU. Most mass will join the dark matter powered protostar via a disk once  $m_{*d} \gtrsim$  a few solar masses.

If the initial protostar fails to accumulate any additional dark matter and retains what it has during Kelvin-Helmholz contraction (which is expected since the contraction time is much longer than the dynamical time), then, ignoring depletion (discussed below, but which occurs on timescales much longer than the initial accretion growth time), the WIMP annihilation luminosity of the star is approximately described by

$$L_\chi \simeq L_{\chi,0} \left( \frac{r_*}{r_{*,0}} \right)^{-3}, \quad (19)$$

where  $L_{\chi,0} \simeq 10^3 L_\odot$  and  $r_{*,0} \simeq 10$  AU are fiducial values for the initial luminosity and radius of the star, respectively, and assuming homologous evolution of the density profile. The protostellar size in models with  $L_\chi = 0$  is expected to be  $\sim 1$  AU for  $m_* \lesssim 10 M_\odot$  (Tan & McKee 2004). Compressing a protostar to this size would lead to  $L_\chi \simeq 10^6 L_\odot$  for the above starting conditions, which is enough luminosity to support a  $\sim 100 M_\odot$  star. So in this case the protostar would be able to be supported by WIMP annihilation giving it  $\gtrsim$  AU sizes until about  $100 M_\odot$ . The ZAMS radius of a  $100 M_\odot$  star is about  $4 R_\odot = 0.02$  AU, so it is clear that contraction to this scale would not be possible until very large stellar masses, unless the WIMP content of the protostar became depleted.

These conclusions are of course sensitive to the initial condition. We expect  $L_{\chi,0} \simeq 10^3 L_\odot$  to be relatively robust as it is set by the baryonic cooling properties of the halo, but the initial size of the dark matter core that provides this WIMP annihilation luminosity depends quite sensitively on the uncertain WIMP mass and the spatial distribution of the dark matter. For example, if the dark matter core has an initial size of about 1 AU (e.g. similar to simulation B, DM fit#2,  $m_\chi = 100$  GeV and models with  $m_\chi = 1$  TeV) and assuming the initial protostellar size scales proportionately and is also about equal to this size, then the potential luminosity available from contraction of the protostar to a given radius would be a thousand times less than the case considered above. Nevertheless, a contraction to  $10 R_\odot$  from 1 AU, would still lead to a WIMP annihilation luminosity of  $8 \times 10^6 L_\odot$ .

We now compare the growth time of the protostar (i.e. the time since its formation, its age),  $t_* = 2.92 \times 10^4 K'^{-15/7} (m_*/100 M_\odot)^{10/7}$  yr (Tan & McKee 2004) to the WIMP depletion time:

$$t_{\text{dep}} = \frac{\rho_\chi}{\dot{\rho}_\chi} \simeq \frac{m_\chi}{\rho_\chi < \sigma_a v >} \rightarrow 105 \frac{m_\chi}{100 \text{ GeV}} \left( \frac{\rho_\chi}{10^{12} \text{ GeV cm}^{-3}} \right)^{-1} \text{ Myr.} \quad (20)$$

If the protostar contracts from an initial radius of 10 AU (where we find  $\rho_\chi \simeq 10^{12} \text{ GeV cm}^{-3}$ , see above) to 1 AU then  $t_{\text{dep}} \simeq 10^5$  yr. We see that, if replenishment of WIMPs in the protostar is negligible, then depletion can become important for AU scale protostars of  $\sim 100 M_\odot$ . These timescales are sensitive to  $m_\chi$  and the dark matter density in the initial equilibrium core, which shows significant variation between simulation A, B, and C.

#### 4. CONCLUSIONS

We have investigated the effects of WIMP dark matter annihilation on the formation of Population III.1 stars by analyzing the results of cosmological simulations that follow the gravitational collapse of baryons and dark matter. While these simulations (O'Shea & Norman 2007; Yoshida et al. 2006) have followed the baryons to very high densities at scales  $\lesssim 1$  AU, the dark matter is only well-resolved down to scales  $\sim 1$  pc. Thus we have considered various power law extrapolations of the dark matter density profile towards the center.

If one assumes the dark matter profile is self-similar, extending inwards from the dark matter dominated regime with  $\rho_\chi \propto r^{-\alpha_\chi}$  and  $\alpha_\chi \simeq 1.5$ , then, for a fiducial WIMP mass of 100 GeV, the dark matter annihilation heating is typically negligible ( $\sim 10^{-4}$  of the cooling rate). This conclusion would be unchanged for a reduction in the WIMP mass by a factor of 10 or more. One of the simulated minihalos (C) exhibits a slightly steeper density profile in the well-resolved region ( $\alpha_\chi = 1.65$ , and in this case WIMP annihilation heating does become important at  $n_H \gtrsim 10^{15} \text{ cm}^{-3}$ ).

However, there are theoretical reasons to expect that the dark matter density profile will steepen because of adiabatic contraction in the baryon-dominated core. Indeed, this process appears to be occurring in the simulations of O'Shea & Norman (2007), although it is not well-resolved. A value of  $\alpha_\chi \simeq 2.0$  appears to be a better description of the dark matter density profile in this region. For such a profile, and again for a 100 GeV particle, the dark matter annihilation heating now exceeds baryonic cooling for densities  $n_H > 10^{14} \text{ cm}^{-3}$ , in agreement with the previous study of Spolyar et al. (2008).

We considered the properties of equilibrium halos in which the density distributions of the baryons and dark matter exhibit a constant density central core. The luminosity that is generated is  $\sim 10^3 L_\odot$  and is relatively invariant, being set by baryonic cooling processes. The sizes of the central cores range from  $\sim 1$  to 40 AU.

The detailed effects of this extra heating on the protostellar structure remain to be determined. We expect that subsequent baryonic growth of the protostar will occur more rapidly than its accumulation of dark matter, because the baryons are undergoing rapid free fall collapse followed by disk accretion. However, even if the initial protostar does not gain any additional dark matter, its initial dark matter content in the subsolar mass core could be sufficient to prevent contraction to the zero age main sequence for masses of  $100 M_\odot$  or greater. Such circumstances could have dramatic implications for the masses of Pop III.1 stars, conceivably raising the mass scale to a regime important for the formation of supermassive black holes. These conclusions depend sensitively on the initial protostellar core, which now needs to be studied with self-consistent cosmological simulations that include the influence of WIMP annihilation heating on the baryons.

We thank T. Abel, K. Freese, C. McKee, D. Spolyar, and N. Yoshida for discussions. The research of JCT is supported by NSF CAREER grant AST-0645412. A.N. acknowledges financial support from the Deutsche Forschungsgemeinschaft (DFG) International Research Training Group GRK 881.

#### REFERENCES

- Abel, T., Bryan, G. L., & Norman, M. L. 2002, *Science*, 295, 93  
 Ascasibar, Y., 2007, *A&A*, 462, L65  
 Bergström, L., Ullio, P. & Buckley, J. H., 1998, *Astroparticle Physics*, 9, 137  
 Blumenthal, G. R., Faber, S. M., Flores, R., & Primack, J. R. 1986, *ApJ*, 301, 27  
 Bromm, V., Coppi, P. S., & Larson, R. B. 2002, *ApJ*, 564, 23  
 Efsthathiou, G., Davis, M., White, S. D. M., & Frenk, C. S., 1985, *ApJS*, 57, 241  
 Eisenstein, D. J. & Hu, W., 1999, *ApJ*, 511, 5  
 Feng, J. L., Matchev, K. T., & Wilczek, F., 2001, *Phys. Rev. D* 63, 045024  
 Freese, K., Bodelheimer, P., Spolyar, D. & Gondolo, P. 2008c, arXiv:0806.0617  
 Freese, K., Gondolo, P., Sellwood, J. A. & Spolyar, D. 2008b, arXiv:0805.3540  
 Freese, K., Spolyar, D. & Aguirre, A. 2008a, arXiv:0802.1724  
 Hall, J. & Gondolo, P., 2006, *Phys. Rev. D* 74, 063511  
 Hockney, R. W. & Eastwood, J. W., 1998, *Computer Simulation using Particles* (Bristol: IOP)  
 Hollenbach, D. & McKee, C. F. 1979, *ApJS*, 41, 555  
 Iocco, F., 2008, *ApJ*, 677, L1  
 Jungman, G., Kamionkowski, M., & Griest, K., 1996, *Physics Reports*, 267, 195  
 McKee, C. F., & Tan, J. C., 2008, *ApJ*, 681, 771  
 Navarro, J. F., Frenk, C. S. & White, S. 1996, *ApJ*, 462, 563  
 Omukai, K., & Palla, F. 2003, *ApJ*, 589, 677  
 O'Shea, B. W., Bryan, G., Bordner, J., Norman, M. L., Abel, T., Harkness, R., & Kritsuk, A. 2004, in "Adaptive Mesh Refinement - Theory and Applications", Eds. T. Plewa, T. Linde & V. G. Weirs, Springer Lecture Notes in Computational Science and Engineering, 2004 (astro-ph/0403044)  
 O'Shea, B. W., McKee, C. F., Heger, A., & Abel, T. 2008, in *First Stars III*, eds. B. W. O'Shea, A. Heger & T. Abel (arXiv:0801.2124)  
 O'Shea, B. W. & Norman, M. L., 2007, *ApJ*, 654, 66  
 Peskin, M. & Schroeder, D. V., 1995, Westview Press  
 Ripamonti, E., Mapelli, M., & Ferrara, A., 2007, *MNRAS*, 375, 1399  
 Spolyar, D., Freese, K., & Gondolo, P., 2008, *Physical Review Letters*, 100, 051101  
 Tan, J. C., & Blackman, E. G. 2004, *ApJ*, 603, 401  
 Tan, J. C., & McKee, C. F. 2004, *ApJ*, 603, 383  
 Taoso, M., Bertone, G., Meynet, G., & Ekstrom, S. 2008, arXiv:0806.2681  
 Yoshida, N., Omukai, K., Hernquist, L., & Abel, T., 2006, *ApJ*, 652, 6  
 Yoon, S.-C., Iocco, F., Akiyama, S. 2008, *ApJ*, submitted, arXiv:0806.2662.